

RESEARCH ARTICLE

10.1029/2018JE005604

Key Points:

- Lunar swirl morphology suggests finely structured near-surface magnetic fields, requiring narrow, shallow magnetic source bodies
- The source bodies underlying swirls must be much more strongly magnetized than is typical of lunar mare basalts
- The inferred source geometry and magnetization could be explained both by magmatic intrusions and associated thermochemical alteration

Correspondence to:

D. J. Hemingway,
djheming@berkeley.edu

Citation:

Hemingway, D. J., & Tikoo, S. M. (2018). Lunar swirl morphology constrains the geometry, magnetization, and origins of lunar magnetic anomalies. *Journal of Geophysical Research: Planets*, 123. <https://doi.org/10.1029/2018JE005604>

Received 3 MAR 2018

Accepted 18 JUL 2018

Accepted article online 26 JUL 2018

Lunar Swirl Morphology Constrains the Geometry, Magnetization, and Origins of Lunar Magnetic Anomalies

Douglas J. Hemingway¹  and Sonia M. Tikoo² 

¹Department of Earth and Planetary Science, University of California, Berkeley, Berkeley, CA, USA, ²Department of Earth and Planetary Sciences, State University of New Jersey, Rutgers, Piscataway, NJ, USA

Abstract Lunar swirls are collections of finely structured bright and dark surface markings, alternating over length scales of typically 1–5 km. If swirls are the result of plasma interactions with crustal magnetic anomalies or electrostatic or magnetic sorting of fine materials, the magnetic field orientation must vary over similar length scales. This requires that the associated source bodies be both shallow and narrow in horizontal extent. The correspondingly restricted volume of the source bodies in turn implies strong rock magnetization. Here we show that if ~300-nT surface fields are necessary to produce observable swirl markings, the required rock magnetization must be > 0.5 A/m, even for very shallow sources and likely closer to ~ 2 A/m or more. This strong source rock magnetization, together with the geometric constraints that favor magmatic structures such as dikes or lava tubes, requires a mechanism to enhance the magnetic carrying capacity of the rocks. We propose that heating associated with magmatic activity could thermochemically alter host rocks and impart them with magnetizations an order of magnitude stronger than is typical of lunar mare basalts. Our results both place constraints on the geometry and magnetization of the source bodies and provide clues about the possible origins of the Moon's crustal magnetic anomalies.

Plain Language Summary Lunar swirls are collections of finely structured, bright and dark surface markings, alternating over length scales of typically 1–5 km. Swirls are thought to form where local magnetic fields shield parts of the lunar surface from exposure to the solar wind or where those magnetic fields lead to sorting of some of the finest lunar soils. In either case, the length scales of swirls are effectively telling us about the structure of near-surface magnetic fields on scales that are finer than what can be measured from lunar orbit. Here we use this length scale information, along with estimates of the strength of those magnetic fields, to obtain new constraints on the underlying magnetized rocks, showing that they must be shallow, narrow, and strongly magnetized. This result helps us to better understand the origin of these magnetized rocks and the history of lunar magnetism more generally. In particular, we suggest that these rocks were likely injected into the crust in the form of dikes or subsurface channels of flowing lava and that they cooled slowly, leading to enhancement of their metal content and enabling the rocks to capture a stable record of the Moon's ancient global magnetic field.

1. Introduction

1.1. Lunar Magnetism Background

Although the Moon does not have an internally generated global magnetic field today, paleomagnetic analysis of Apollo samples shows that many lunar rocks exhibit a thermoremanent magnetization (TRM), implying that a long-lived global field was present early (before ~1–2.5 Ga) in the Moon's history (e.g., Tikoo et al., 2017; Weiss & Tikoo, 2014); during the period ~3.85–3.56 Ga, lunar surface fields are inferred to have reached intensities of $78 \pm 43 \mu\text{T}$ (comparable to the Earth's modern field).

In situ Apollo magnetometer observations found surface fields as large as 327 nT at the Apollo 16 landing site (Dyal et al., 1974). Magnetometer and electron reflectometer experiments aboard orbiting spacecraft (the Apollo 15/16 subsatellites, Lunar Prospector, and Kaguya), however, have revealed that other portions of the lunar crust are even more strongly magnetized (e.g., Mitchell et al., 2008; Purucker & Nicholas, 2010; Richmond & Hood, 2008; Tsunakawa et al., 2015). These orbit-based measurements necessarily miss the finest structures in the near-surface magnetic fields and therefore provide only lower bounds on the magnitude of surface

fields (Halekas et al., 2010). For instance, using downward continuation techniques, Tsunakawa et al. (2015) estimate a surface field of ~ 20 nT at the Apollo 16 landing site—more than an order of magnitude less than what was measured in situ. Meanwhile, the same technique estimates surface fields of > 200 nT at the Descartes magnetic anomaly (~ 50 km away) and more than 500 nT in a number of other locations, such as at Reiner Gamma. Given that even these estimates may be an order of magnitude too small, it is not unreasonable to expect strong crustal magnetic anomalies to exhibit surface fields of thousands of nanoteslas (Halekas et al., 2010; Hemingway & Garrick-Bethell, 2012). In principle, the technique of electron reflectometry (Halekas et al., 2001; Mitchell et al., 2008) can be used to determine the magnetic field strength at the surface, but the technique has limited sensitivity to surface fields that vary over short length scales ($< \sim 10$ km; Halekas et al., 2010). Accordingly, surface field estimates from electron reflectometry (Mitchell et al., 2008) are similar to the magnetometer-based results of Tsunakawa et al. (2015), with both effectively missing the finer structures where surface fields may be strongest (Halekas et al., 2010).

Several ideas have been proposed to explain how the Moon might have generated and sustained an intrinsic dynamo field that could have magnetized parts of the crust (e.g., Dwyer et al., 2011; Evans et al., 2014; Laneuville et al., 2014; Le Bars et al., 2011; Scheinberg et al., 2015, 2018; Stegman et al., 2003), but it remains a challenge to explain how even the weakly magnetized Apollo samples acquired their magnetization from such a field because most lunar thermal evolution models predict dynamo-driven surface fields well below the inferred ~ 100 μ T (Weiss & Tikoo, 2014). The origins of the much stronger, localized crustal magnetic anomalies are even more puzzling. Some studies suggest that very strong transient fields may have magnetized parts of the crust during basin-forming impact events (e.g., Hood & Artemieva, 2008; Mitchell et al., 2008), while others suggest that the localized crustal anomalies are related to the emplacement of especially iron-rich exogenic materials (Wieczorek et al., 2012) or intrusions (Purucker et al., 2012). Distinguishing between the possible formation mechanisms has been difficult due in part to our limited knowledge about the near-surface field structure and the geometry of the underlying magnetic source bodies. Putting constraints on these aspects of crustal magnetic sources could provide valuable insights into their possible origins and, in turn, the thermal history and evolution of the Moon.

1.2. Exploiting Lunar Swirls

Another intriguing aspect of the Moon's crustal magnetic anomalies is that many of them are colocated with peculiar clusters of optical anomalies, comprising alternating bright and dark markings, known as lunar swirls (Figure 1; e.g., Blewett et al., 2011; Denevi et al., 2016; El-Baz, 1972). One possible explanation for the formation of swirls is that they are the result of spatially variable space weathering that occurs due to magnetic deflection of the incoming solar wind (e.g., Hood & Schubert, 1980; Hood & Williams, 1989), which is known to affect the optical properties of exposed surfaces over time (e.g., Hapke, 2001; Noble et al., 2001). Roughly speaking, portions of the surface with open magnetic field lines may be expected to experience normal or even accelerated solar wind-related space weathering, leading to darkening, whereas portions of the surface beneath closed magnetic field lines should experience greater protection from solar wind weathering, thus remaining relatively bright (Hemingway & Garrick-Bethell, 2012). Indeed, magnetometer-based studies of magnetic field structure (Hemingway & Garrick-Bethell, 2012; Shibuya et al., 2010; Tsunakawa et al., 2015), as well as hybrid and kinetic plasma simulations (e.g., Bamford et al., 2012, 2016; Deca et al., 2015, 2016; Fatemi et al., 2015; Giacalone & Hood, 2015; Jarvinen et al., 2014; Poppe et al., 2012, 2016; Zimmerman et al., 2015), indicate that swirl morphology may be dictated by magnetic field topology in precisely this way. It has also been proposed that swirls may be the result of electrostatic (Garrick-Bethell et al., 2011) or magnetic (Pieters et al., 2014) sorting of fine-grained materials, rather than of deflection of solar wind. In this case, the near-surface magnetic field structure dictates the spatial variation in the forces responsible for the sorting and should thus be tightly linked to the structure of the resulting optical anomaly. The connection between swirl morphology and field topology is less obvious under the hypothesis that swirls are the result of scouring due to cometary impacts (see Schultz & Srnka, 1980; Syal & Schultz, 2015), though even in that model, it remains possible that the near-surface field structure would play a role in determining the way the impacting material interacts with and affects the optical properties of the surface. In any case, we will proceed here on the assumption that there is a close connection between the near-surface magnetic field structure and the morphology of the swirls. That is, following Hemingway and Garrick-Bethell (2012), we will use swirl morphology as a proxy for the structure of the near-surface magnetic fields.

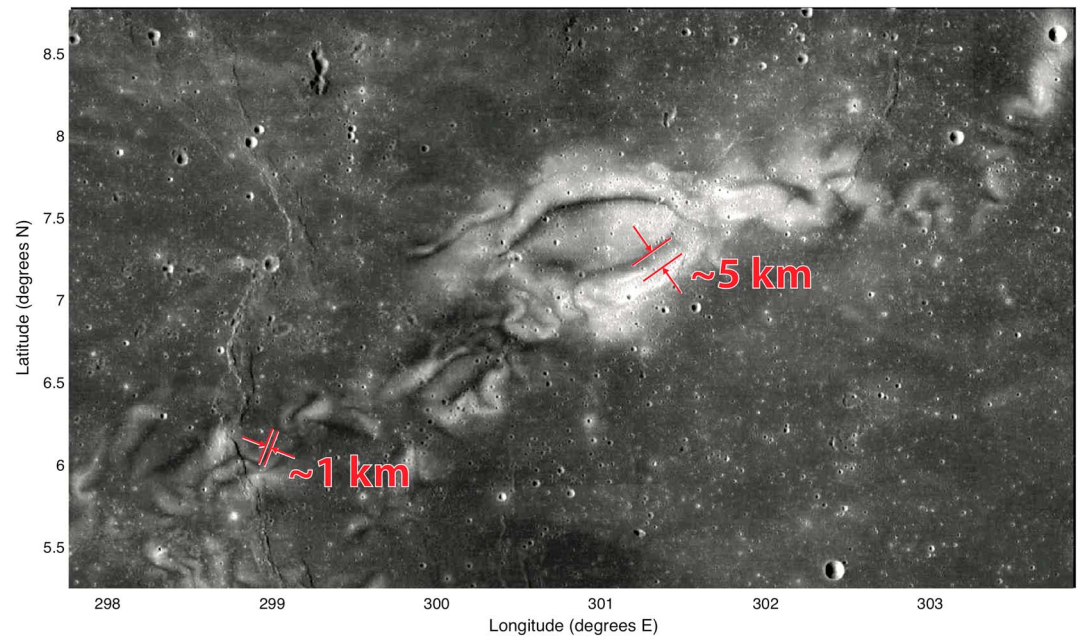


Figure 1. The archetypal lunar swirl complex—Reiner Gamma—consisting of numerous alternating bands of bright lobes and dark lanes. The largest features have bright-to-dark transition length scales of up to ~ 5 km, but much more finely structured features are discernible as well. Image is from the Lunar Reconnaissance Orbiter Camera Wide Angle Camera (Mahanti et al., 2016; Robinson et al., 2010; Speyerer et al., 2012).

1.3. Outline

In section 2, we develop a model and combine it with observations to place constraints on the geometries and magnetizations of the source bodies associated with lunar swirls. We discuss the implications of these results for the distribution of swirls and the possible origins of these crustal magnetic anomalies, showing that unusually intense rock magnetization is required. In section 3, we explore mechanisms by which these intense rock magnetizations could be realized through magnetic enhancement associated with heating due to the emplacement of dikes or lava tubes in the reducing environment of the shallow subsurface. Finally, we provide concluding remarks and discuss future work in section 4.

2. Constraining Source Geometry and Magnetization

2.1. Model Description

Here we wish to relate the near-surface magnetic field structure, parameterized by what we call the transition length scale (L , see below), and the estimated surface field strength (B) to the source body's magnetization (or magnetic moment per unit volume, M) and the geometry of the underlying magnetized source body. Following Hemingway and Garrick-Bethell (2012), we will assume that the bright-to-dark transition length scale found at lunar swirls can be used as a proxy for the length scale over which the near-surface magnetic field direction transitions from vertical (perpendicular to the surface) to horizontal (parallel to the surface). More precisely, we will define this bright-to-dark transition length scale as the distance between the brightest part of a bright lobe and the darkest part of the adjacent dark lane as measured by albedo profiles taken perpendicular to the long axis of the feature (Figure 2). Although large swirl complexes, such as the archetypal Reiner Gamma, can span several tens of kilometers, they are invariably ensembles of smaller, elongate structures, with the transition from bright to dark taking place over distances of typically 1–5 km (Figure 1). We call this transition length scale L , and we use the term interchangeably to describe both the optical bright-to-dark transition and the magnetic field's vertical-to-horizontal transition (Figure 2).

Given the elongate nature of the finest structures in swirl complexes, we model the underlying sources as elongate structures. Our model sources are buried rectangular prisms that, for the sake of simplicity, are infinitely long. This simplifies the expressions, reducing the problem to two dimensions, and is a reasonable approximation when examining areas far from the ends of the source. We focus on a cross section through the surface and the underlying source body, which we take to have height h , width w , and whose top is at a depth d

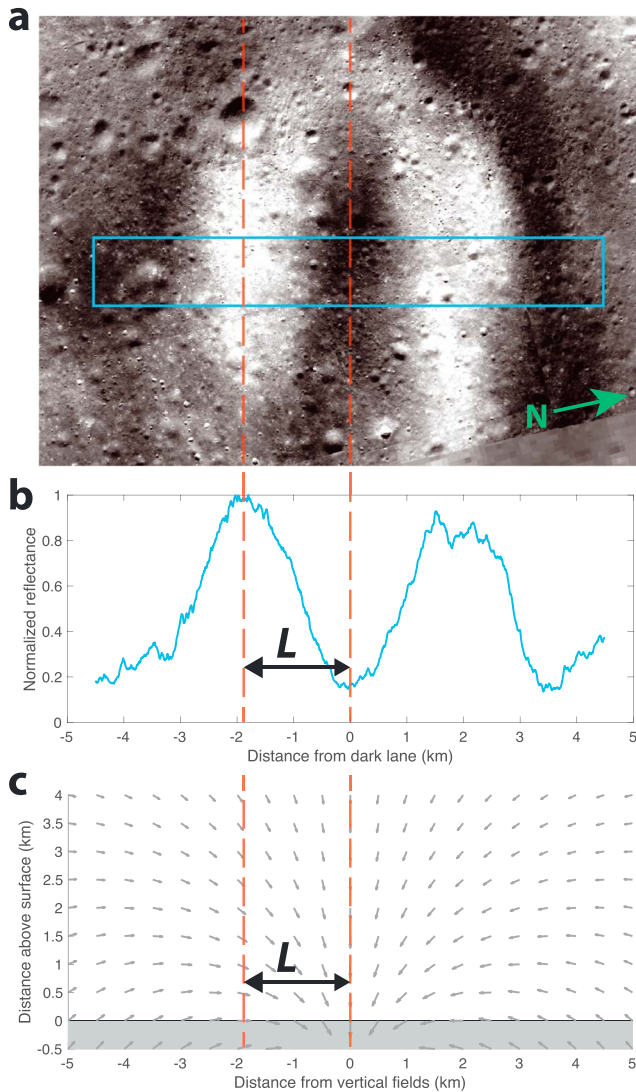


Figure 2. Illustration of the transition length scale, L . (a) Close-up of a lunar swirl centered on its dark lane (this particular feature is located at 17.4°N , 87.6°E). (b) Reflectance profile across the bright and dark parts of the swirl, based on the pixels in the blue box illustrated in (a), with reflectance normalized to the brightest part of the swirl. The transition length (L) from the brightest part of the bright lobe to the center of the adjacent dark lane is indicated. (c) Vertical cross section illustrating notional magnetic field vectors, with the near-surface field direction transitioning from vertical to horizontal over a distance L . Image in (a) is from the Lunar Reconnaissance Orbiter Camera Narrow Angle Camera (Humm et al., 2016; Robinson et al., 2010; Speyerer et al., 2012).

(2) into (1) allows the problem to be fully described in terms of the surface field strength per unit magnetization (B/M) and the dimensionless quantities of the prism's aspect ratio (h/w) and its relative burial depth (d/L).

2.2. Model Results

It follows from (2) that the source depth can never be greater than the transition length scale ($d < L$) and that the width of the source can never exceed twice the transition length scale ($w < 2L$). Hence, the sources must be both shallow and narrow in order to produce the transition length scales observed at lunar swirls ($L \approx 1\text{--}5$ km). Similarly, it follows that, in order to preserve the transition length scale at the surface (L), as the depth to the top of the source increases, the source must become increasingly compact (Figure 4a), with

beneath the surface (Figure 3). In principle, we can model source bodies with arbitrarily more complicated cross sections by superimposing a series of such prisms. Likewise, it is possible to model collections of separate but nearby sources, which may produce complicated surface fields. For clarity and simplicity, however, we will focus for now on the case of a single rectangular prism. If the source is not unidirectionally magnetized, the field structure may be highly complex near the source but, due to partial mutual cancellation of distinctly oriented adjacent magnetic moments, will reduce to weaker and smoother fields with increasing distance from the source. From the perspective of constraining source rock magnetization, the assumption of unidirectional magnetization is thus conservative in that it demands the least in terms of source rock magnetization. Although any magnetization direction is possible, we will focus on the two end member cases of horizontal (parallel to the surface) and vertical (perpendicular to the surface) magnetization. We also restrict the magnetization direction to be perpendicular to the long axis of the source. That is, the magnetization direction is assumed to lie within the plane of Figure 3. This is broadly consistent with previous inversions for isolated, swirl-bearing magnetic anomalies such as Airy and Reiner Gamma (e.g., Hemingway & Garrick-Bethell, 2012; Kurata et al., 2005; Oliveira & Wieczorek, 2017). Moreover, in the limit of an infinitely long source, magnetization components parallel to the long axis (i.e., out of the plane of Figure 3) do not contribute to the external magnetic field and hence have no effect on the geometric constraints we derive below.

Under these assumptions, it can be shown (Appendix A) that the magnitude of the surface field strength per unit magnetization, measured directly above the source, is given by

$$\frac{B}{M} = \frac{\mu_0}{\pi} \left(\arctan \left(\frac{d+h}{w/2} \right) - \arctan \left(\frac{d}{w/2} \right) \right) \quad (1)$$

where the depth to width ratio (d/w) is constrained by the transition length scale (L) according to the geometric relationship

$$L = \sqrt{(d+h)d + (w/2)^2} \quad (2)$$

(see Appendix A for details). Equation (1) is obtained by integrating the dipole field equation (A1) over the volume of the prism illustrated in Figure 3. In the case of horizontal magnetization, we obtain the transition length scale by solving (A4) for the position where the field becomes vertical at the surface. Similarly, in the case of vertical magnetization, we obtain the transition length scale by solving (A13) for the position where the field becomes horizontal at the surface. Owing to symmetries in the established problem geometry, (1) and (2) hold regardless of whether the magnetization direction is horizontal or vertical. Rearrangement and substitution of

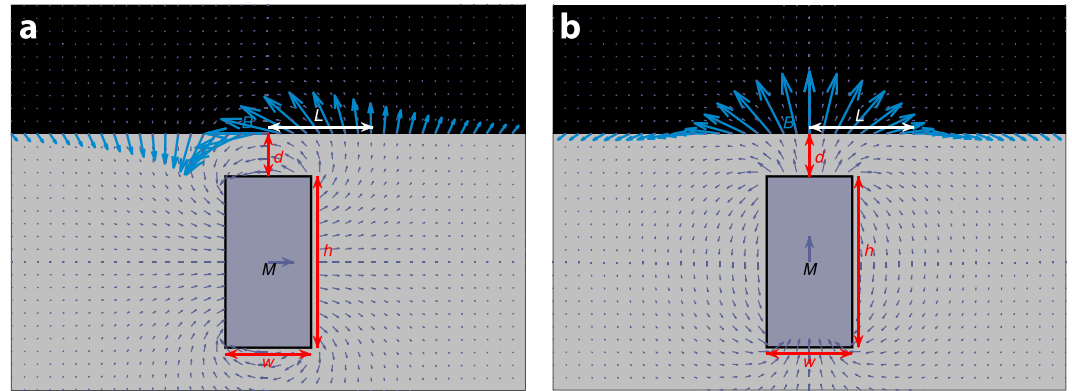


Figure 3. Model cross section of buried magnetized rectangular prism illustrating the relationship between its width (w), height (h), burial depth (d), and the length scale (L) over which the surface field orientation transitions between vertical and horizontal. The surface field strength directly above the source (B) and the source magnetization (M) are also indicated. Field vectors are shown over a regular grid with the surface field vectors exaggerated for emphasis. The two panels illustrate the cases of horizontal (a) and vertical (b) magnetization.

the precise relationship depending in part on the prism's aspect ratio. The implied rock magnetization thus increases with increasing burial depth and, equivalently, with decreasing source width (Figure 4b).

Considering a range of possible aspect ratios and relative burial depths, we can compute from (1) the magnitude of the surface field per unit magnetization in the source body (Figure 5a). Conversely, we can solve (1) for the source magnetization required to produce a given surface field (Figure 5b) across the same parameter space. The rock magnetization required to account for the observed surface fields increases with relative burial depth and becomes impossibly large as the burial depth approaches the transition length scale. But even in the limit of an infinitely tall prism, with zero burial depth, the required magnetization is still

$$\frac{M}{B} = \frac{2}{\mu_0} \approx 0.159 \frac{(\text{A/m})}{(100\text{nT})} \quad (3)$$

Given that the surface field estimates of Tsunakawa et al. (2015) provide only a lower bound and given the theoretical arguments given by Halekas et al. (2010) and Hemingway and Garrick-Bethell (2012), we will take 300 nT to be a conservative estimate of the surface fields present where swirls are found. Given this assumption, equation (3) and Figure 5 demonstrate that rock magnetization at swirl-forming magnetic anomalies

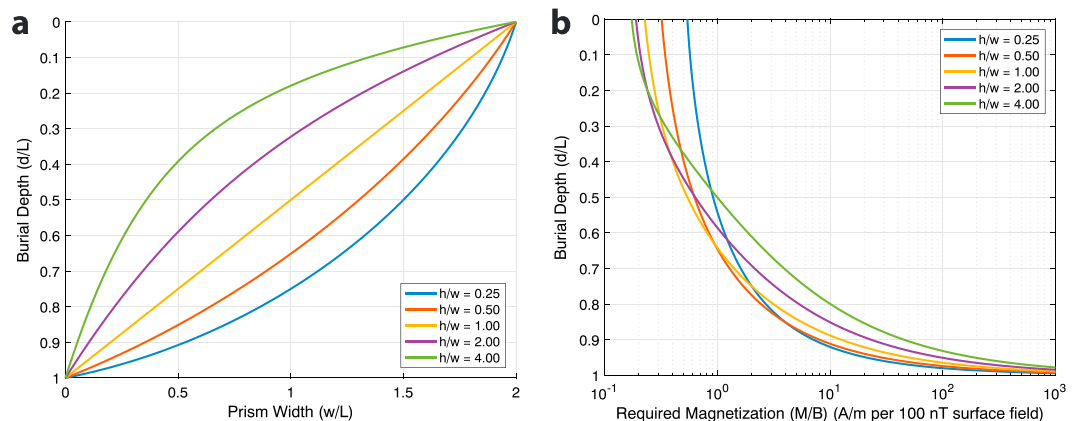


Figure 4. Relationship between relative burial depth (d/L), relative source width (w/L), and relative required magnetization (M/B) for various aspect ratios (h/w). (a) The maximum burial depth (d) is equal to the transition length scale (L) and requires an infinitely compact source ($w \rightarrow 0$). The maximum source width (w) is twice the transition length scale (L) and requires the top of the source to be at the surface ($d = 0$). (b) In the shallow source limit of $d = 0$, the required magnetization is determined by equation (1), is entirely a function of aspect ratio, and reaches its minimum value of $\approx 0.159 (\text{A/m})/(100 \text{ nT})$ for an infinitely tall source ($h/w \rightarrow \infty$). As relative burial depth (d/L) increases, the relative required magnetization (M/B) increases rapidly, becoming infinite as the burial depth approaches its maximum value ($d/L \rightarrow 1$) and the source becomes infinitely compact ($w \rightarrow 0$).

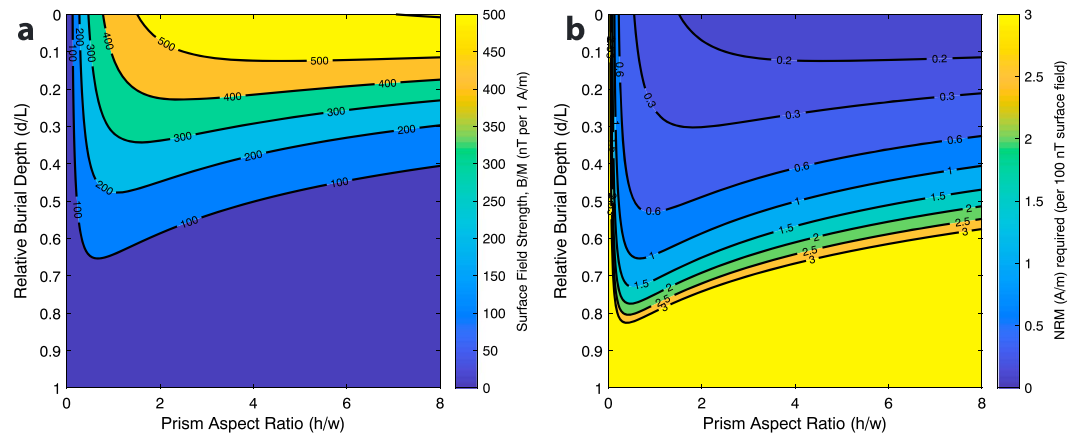


Figure 5. Surface field strength and required magnetization as a function of source geometry. (a) Surface field strength drops rapidly as relative burial depth (d/L) increases and as the prism's aspect ratio (h/w) becomes very small. (b) Required source magnetization per 100-nT surface field. The required magnetization increases rapidly as relative burial depth (d/L) increases and as the prism's aspect ratio (h/w) becomes very small.

must be at least ~ 0.5 A/m, even for zero depth sources, and ~ 2 A/m for sources that are buried by a depth of more than half the transition length scale (i.e., buried more than 0.5–2.5 km beneath the surface). For surface fields of $> 1,000$ nT, the corresponding values are more than 1.5 and 6 A/m, respectively. If the source is more deeply buried (i.e., larger d/L), or has a larger aspect ratio (h/w), as expected for dikes, the implied rock magnetization could easily exceed several amperes per meter (Figure 5b).

2.3. Implications for Swirl Distribution

A long-standing question has been: why is it that swirls are found at many, but not all, of the localized crustal magnetic anomalies? Our analysis suggests that part of the answer may have to do with the burial depth of the magnetized source bodies. It is intuitive, and Figure 5 makes it clear that, for a given rock magnetization, the surface field strength drops off rapidly with burial depth. Hence, if the formation of swirls requires very strong surface fields, then deep sources will be unable to produce swirls.

What is perhaps less obvious is that the geometric relationship expressed in equation (2) also implies that any magnetic source capable of producing swirls, with their characteristic bright-to-dark transition taking place over no more than a few kilometers, must be both narrow (less than a few kilometers wide) and shallow (within a few kilometers of the surface). Deeper sources produce surface fields that are not only weaker, for a given source magnetization, but also whose orientations vary only gradually across the surface. Without the strong and spatially rapid changes in surface field direction that arise from narrow, shallow sources, the formation of swirls may be impossible.

Indeed, a comparison between the locations of swirls, as mapped by Denevi et al. (2016), and an estimate of the depth to the top of all the crustal magnetic sources globally (Wieczorek, 2018) confirms that swirls tend to be found only in places where the magnetic sources are closest to the surface (Figure 6a). The Crisium basin, for example, features two strong magnetic anomalies, but, because the depth to the top of the source is more than ~ 15 km, the surface fields must be relatively weak and their orientation must vary only gradually across the surface, precluding the formation of swirls. More generally, whereas the global distribution of source depths is broad and centered on a depth of ~ 10 km, swirl regions are strongly biased toward shallow sources (Figure 6b). Not surprisingly, swirls also tend to be found in regions where the magnetic field strength is relatively high (Figure 6c).

2.4. Implications for Origin Scenarios

There are several forms of remanence that could account for the natural remanent magnetization (NRM) found in parts of the lunar crust, including TRM, whereby the initially hot source materials cool through the ferromagnetic grains' Curie temperature in the presence of an ambient magnetic field; thermochemical remanent magnetization (TCRM), where new magnetic carriers are formed or existing carriers are altered due to exposure to high temperatures; shock remanent magnetization (SRM), involving remagnetization of grains due to transient high pressures accompanying impact shock waves; and/or isothermal remanent magnetization

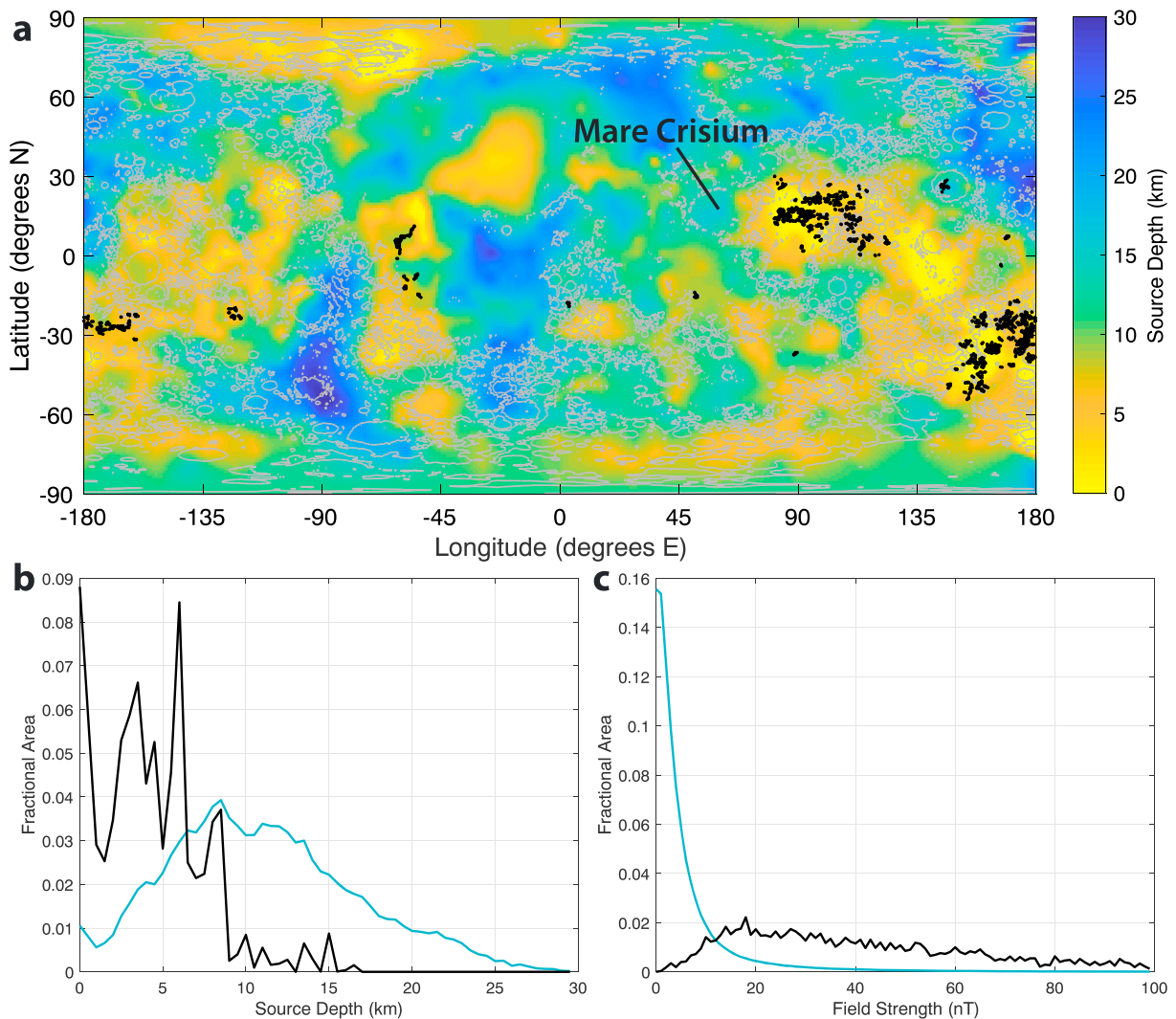


Figure 6. Lunar swirls and magnetic source depths. (a) Map showing the depth to the top of the magnetic source material as estimated by Wieczorek (2018), with black overlay indicating the locations of lunar swirls as mapped by Denevi et al. (2016). Gray contours are derived from LOLA topography and are included for geographic context. (b) Area-weighted histograms of source depth showing that swirls (black) tend to correspond to regions with source depths that are shallow compared to the overall distribution (blue). (c) Area-weighted histograms of field strength showing that, whereas field strength is low over the vast majority of the surface (blue), swirls (black) tend to be found where field strength is relatively high. Recall that the field strength estimates of Tsunakawa et al. (2015) may be an order of magnitude too small at strong crustal magnetic anomalies and that this effect is compounded by the map's limited resolution of 5 pixels per degree.

(IRM), which involves exposure to transient magnetic fields with intensities far in excess of any likely long-lived ambient fields. In order to understand the origins of the magnetic anomalies accompanying swirls in particular, the challenge is to identify processes that can account for not only the inferred intensity of magnetization but also the geometric constraints.

Depending on lithology, endogenic lunar rocks in the sample record typically have saturation remanent magnetizations (M_{rs}) ranging between 0.05 A/m (feldspathic highland rocks) and 30 A/m (mafic impact melt breccias; Wieczorek et al., 2012). Assuming a TRM acquired during primary cooling, we can estimate the expected NRM (M_{nr}) intensity according to

$$M_{nr} = \frac{BM_{rs}}{a} \quad (4)$$

where B is the paleofield intensity and a is a calibration constant with a value of $\sim 3000 \mu\text{T}$ (though this value is uncertain by a factor of 2–3; Gattacceca & Rochette, 2004; Weiss & Tikoo, 2014). Paleomagnetic studies suggest that surface fields on the Moon were likely $< \sim 100 \mu\text{T}$ in intensity for nearly all of lunar history (Weiss & Tikoo, 2014). This implies that, assuming the rocks carry a TRM, the NRM of known lunar materials and

melt breccias are unlikely to exceed ~ 1 A/m, even when utilizing upper limit values for M_{rs} (Figure 7). For comparison, the NRM of most lunar breccia samples are ~ 0.1 A/m and the NRM of most mare basalt samples range between ~ 0.001 and ~ 0.01 A/m (Weiss & Tikoo, 2014). However, given that the Apollo missions only sampled rocks at the lunar surface, and only in a limited number of locations, it is possible that unsampled endogenic lunar materials have higher NRMs and saturation remanent magnetizations.

Impacts can produce strong, transient plasma fields that could have magnetized target rocks via either TRM or SRM (Figure 8). As discussed above, however, endogenic lunar materials may not have sufficiently high iron contents to produce TRMs with the inferred intensity of 0.5–2 A/m. SRM may be even less likely given that the intensity may be more than an order of magnitude weaker than that of TRM produced in an equivalent field (Tikoo et al., 2015). On the other hand, basin-forming impact events could lead to extremely intense transient fields (perhaps ~ 1 mT) near the basin antipode where the most distal ejecta is converging (e.g., Hood & Artemieva, 2008; Srnka, 1977), leading to acquisition of a strong SRM within the ejecta deposits. In general, however, impact-generated fields may be complex as well as time varying, making it difficult for them to impart a coherent remanent magnetization.

Large impactors could also have delivered unusually metal-rich exogenic materials, with the hot ejecta acquiring a TRM that could be much more intense than any produced from endogenic materials (Wieczorek et al., 2012). While such impact ejecta or impact melt scenarios could be consistent with the inferred shallowness of the sources, however, the broad, quasi-circular shapes of impact basins or melt sheets are not consistent with the narrow, elongate source structures we infer for swirls (Figure 8). Ejecta could explain elongate sources, although one might expect rays to be locally parallel and unlike the morphologically complex structures found at swirls (Figure 1).

It has also been suggested that compression of a cometary coma colliding with the Moon could produce transient magnetic fields as intense as 1–100 mT (Schultz & Srnka, 1980; Syal & Schultz, 2015). For ferromagnetic grains within lunar rocks, magnetic coercivity is typically tens of milliteslas (see Table 2 by Rochette et al., 2010), meaning that it may be possible for such strong transient fields to magnetize mare basalts to several amperes per meter. However, it is unclear whether these fields could magnetize a sufficient volume of rock to generate a substantial magnetic moment or whether these fields can have the complex geometries required to make the narrow, elongate structures inferred for swirl-bearing magnetic anomalies. On the other hand, under the cometary impact hypothesis for swirl formation, the source geometry need not closely match swirl morphology (a key assumption in our analysis) since this model proposes that swirls are the result of scouring during the impact event rather than being the result of space weathering or magnetic or electrostatic sorting.

Another possibility is that the sources formed due to magmatic processes, either intrusive, like dikes or lava tubes, or extrusive, such as mare basalt flows. Like impact basins and melt sheets, surface lava flows satisfy the requirement of being shallow sources but are too broad to be consistent with the finely structured surface fields necessary to give rise to swirls (Figure 8). Dike complexes, on the other hand, typically produce linear structures that trend roughly parallel to one another, and can sometimes exhibit curved geometries, as in the case of ladder dikes (e.g., Hodge et al., 2012). It is possible that undiscovered dikes could exist within the upper portions of the lunar crust, especially given that they may not be wide enough to produce density anomalies strong enough to be observable in gravity observations. Subsurface lava tubes, which are likely present within mare plains, should have the shallow depths and narrow, elongate structures expected for the sources underlying lunar swirls. The parent magmas of such dikes and lava tubes would likely be similar in composition to those of mare basalts. The main challenge associated with such source bodies is that, in order to produce the observed strong remanent crustal fields, they would need to contain far more metallic iron than what has so far been reported for mare basalts. In section 3, we explore scenarios in which the emplacement of dikes or lava tubes can lead to enhancement of magnetic carriers (raising the mare basalt NRM values to beyond those in Figure 7) through reduction reactions and thermochemical alteration.

3. Magnetic Enhancement of Lunar Rocks

In section 2.4, we argued that the morphology of swirls is suggestive of magnetic source structures resembling dikes or lava tubes but that the required magnetizations are at least an order of magnitude larger than typical mare basalts in the sample record. Localized magmatism could produce such strong magnetizations within the lunar crust in multiple ways. First, mafic dikes or lava tubes might be sourced from unusually iron-rich

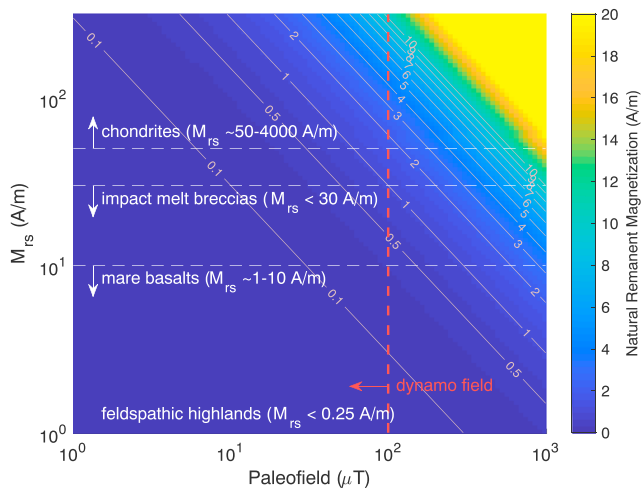


Figure 7. Natural Remanent Magnetization, assuming thermoremanent magnetization, as a function of paleofield and rock type (characterized here by saturation remanent magnetization, M_{rs}).

magmas, thereby producing more metal-rich rocks. Given that the Apollo missions sampled only a limited range of rock types and locations, it is conceivable that more metal-rich endogenic lunar rocks exist in other places that have not yet been explored. Alternatively, the emplacement of dikes and lava tubes may reset the magnetization within immediately adjacent rocks via a baked contact. In this scenario, host rocks next to a baked contact are exposed to very high temperatures that may be sufficient to impart them with full or partial TRM (pTRM) as they cool below their Curie temperatures (Everitt & Clegg, 1962). Heating may also alter the remanent magnetization within rocks via the modification of preexisting ferromagnetic grains or the creation of new ones (e.g., Buchan, 2007; Coe et al., 2014). In the terrestrial environment, emplacement of magmatic products may alter primary titanomagnetite within nearby host rocks, leading to the formation of more oxidized phases such as titanomaghemite. Such subsolidus alteration has been observed in mid-ocean ridge basalts (e.g., Shau et al., 2004). On Earth, water-rock interactions may also lead to hydrothermal alteration of basaltic materials within the seafloor. This process may transform titanomagnetite into more Ti-poor magnetite and ilmenite (e.g., Shau et al., 2000). Alteration of mid-ocean ridge basalt occurs almost immediately after emplacement (Kent & Gee, 1996), and the resulting

TCRM carried by more oxidized phases typically has a weaker magnetization intensity than the original TRM acquired during primary cooling (Xu et al., 1997). In the case of the Moon, heating may produce subsolidus reduction of primary nonferromagnetic minerals such as ilmenite that would lead to the formation of new metallic iron. This process would impart new or altered ferromagnetic grains with TCRM, likely enhancing the original magnetization within the rock.

3.1. Formation of Ferromagnetic Grains in Lunar Rocks

Following Oliveira et al. (2017), and assuming TRM, we determined that the > 0.5 -A/m magnetization intensities we infer for lunar swirl magnetic sources require rocks to have abundances of > 0.3 wt.% Fe and > 31 wt.% Fe, assuming magnetizing field strengths of 100 and 1 μ T, respectively. These Fe abundances are subject to a cumulative factor of ~ 4 uncertainty that is related to (factor of ~ 2) variations in the magnetic hysteresis properties of mare basalts and the (factor of ~ 2) uncertainty in the relationship between magnetizing field intensities and M_{rs} values of Fe-bearing rocks (see Oliveira et al., 2017, section 2.2). For our calculations, we

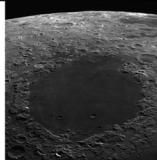
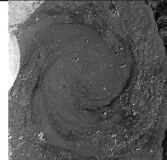
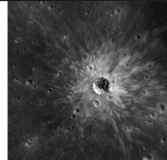
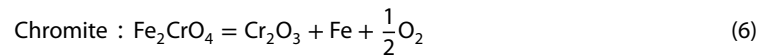
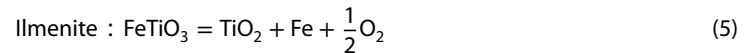
Remanence	TRM or TCRM			SRM	IRM
Potential lunar swirl source bodies	 dikes and lava tubes	 mare basalt flows	 basin impact melt sheets	 impact ejecta and breccias	 comet impacts
Depth ($d < 3$ km)	✓	✓	✓	✓	✓
Morphology ($L < 5$ km)	✓	✗	✗	? asymmetric ejecta deposit?	?
Magnetization (NRM > 0.5 A/m)	? iron-rich dikes or alteration of adjacent rocks?	✗	? exogenic metal?	? exogenic metal?	?

Figure 8. Possible origins of the crustal magnetic anomalies underlying lunar swirls. Listed are several possible source origin scenarios and magnetization processes (TRM is thermoremanent magnetization, TCRM is thermochemical remanent magnetization, SRM is shock remanent magnetization, and IRM is isothermal remanent magnetization) along with the ability of each to satisfy the inferred geometric and intensity constraints (check marks indicate where constraints are satisfied easily; cross marks indicate where constraints are unlikely to be satisfied; question marks indicate where constraints may be met under the right circumstances or where there is no clear conclusion). Image credits: NASA.

used a hysteresis loop squareness of 0.0064 and we assumed that the source rocks had mare basalt-like densities of $3,300 \text{ kg/m}^3$. In the high field ($100 \mu\text{T}$) regime, the required Fe contents are similar to those inferred by Oliveira et al. (2017) for basin impact melt sheets, as well as measured metal contents in melt-bearing lunar impact breccias (Gose & Butler, 1975). While mare basalts typically have lower metal contents of $\sim 0.08 \text{ wt.}\%$ Fe (Gose & Butler, 1975), pervasive reduction of magmatic bodies of similar initial composition may well be capable of generating sufficient Fe to produce magnetizations of $>0.5 \text{ A/m}$ (see below).

Experimental petrology studies indicate that mare basalts generally formed in a reducing environment with oxygen fugacities ($f\text{O}_2$) approximately one log unit below the iron-wüstite buffer (i.e., IW-1; Sato et al., 1973). The reduction of mare materials was likely achieved when their parent magmas ascended to depths $< \sim 8.5 \text{ km}$ (Nicholis & Rutherford, 2009). At these shallow depths (and accompanying low pressures), carbon becomes oxidized to carbon monoxide. The liberation of carbon monoxide causes subsolidus reduction of oxides and silicates and the associated creation of the metallic ferromagnetic minerals observed in lunar rocks (Sato et al., 1973). A number of reduction reactions that are capable of forming metallic iron from different primary mineral phases may take place during deuteric cooling of initially molten material. Some example reaction pathways for different minerals (from Haggerty, 1971) include the following:



The amount of metallic Fe produced by subsolidus reduction during primary cooling will depend on factors such as the initial abundances of precursor minerals (e.g., ilmenite), as well as the cooling rate. Intrusive bodies have longer cooling timescales than mare flows, so it is likely that they would experience more subsolidus reduction than basalts at the lunar surface. Mare basalts on the Moon are often classified into two categories based on Ti content: low Ti and high Ti. The low-Ti basalts tend to have modal mineralogies with $< \sim 8 \text{ vol.}\%$ ilmenite (Dowty et al., 1973; Neal et al., 1994), whereas high-Ti mare basalts have been found with up to $\sim 22 \text{ vol.}\%$ ilmenite (e.g., Longhi et al., 1974). Low-Ti mare basalts are also less dense ($\rho \approx 3,270 \text{ kg/m}^3$) than high-Ti mare basalts ($\rho \approx 3,460 \text{ kg/m}^3$; Kiefer et al., 2012). In the extreme scenario wherein all ilmenite in a rock with high-Ti mare basalt composition (e.g., 22 vol.% ilmenite) is reduced and converted to Fe and TiO_2 , the rock could be enriched with an additional $\sim 11 \text{ wt.}\%$ Fe. Such a concentration of Fe would permit rock magnetizations of $\sim 17.5 \text{ A/m}$ if magnetized in the high field ($100 \mu\text{T}$) regime (Oliveira et al., 2017). Even in a rock with low-Ti basalt composition (e.g., 2 vol.% ilmenite), full breakdown of ilmenite would result in $\sim 1 \text{ wt.}\%$ neoforced Fe (corresponding to $M \approx 1.6 \text{ A/m}$, assuming the high field regime). These Fe contents are at least an order of magnitude higher than those reported for Apollo mare basalt samples (typically $\sim 0.08 \text{ wt.}\%$) (Gose & Butler, 1975). While it is unlikely that all ilmenite would actually experience such a pervasive breakdown in a natural setting, the preceding calculations nevertheless demonstrate the potential for subsolidus reduction to create substantial amounts of metallic Fe, especially in slowly cooled magmatic bodies.

Laboratory heating of mare basalts and synthetic analogs in a controlled oxygen fugacity atmosphere to temperatures up to 800°C has produced subsolidus reduction and the associated growth of metal grains in several paleomagnetism studies. Pearce et al. (1976) conducted a Thellier-Thellier paleointensity experiment (Thellier, 1959) on a synthetic sample intended to approximate mare basalt 10017. During the experiment, the sample was heated in a $\sim 20\% \text{ H}_2$ and $\sim 80\% \text{ N}_2$ mixture that the authors measured (using a yttria-doped zirconia sensor) to have an $f\text{O}_2$ of approximately IW-1 at 800°C . As part of the paleointensity experiment, the sample was heated to increasing temperatures and imparted with a pTRM at each temperature step. At low temperatures, the amount of pTRM gained at each heating step increased steadily. However, between the 700 and 800°C heating steps, the authors observed a >1 order of magnitude increase in the intensity of pTRM gained (Figure 9). The majority of this increase was attributed to an experimentally determined factor of 5 increase in the amount of metallic iron in the sample. This increase in metal content was caused by rapid subsolidus reduction at the rims of ilmenite grains. The neoforced iron would have acquired a TCRM as it cooled. Petrographic analyses of altered ilmenite grains revealed that heating the sample at 800°C for 30 min produced approximately twice as much reduction along the rims of ilmenite grains as a 20-min heating experiment. This indicates that the amount of reduction increases with the duration of heating, although in both cases reduction was limited to the outermost $1\text{--}2 \mu\text{m}$ of ilmenite grains. However, due to the lack of long-term heating experiments on lunar rocks, it is unclear what the rate of transformation of ilmenite is or how long it takes for

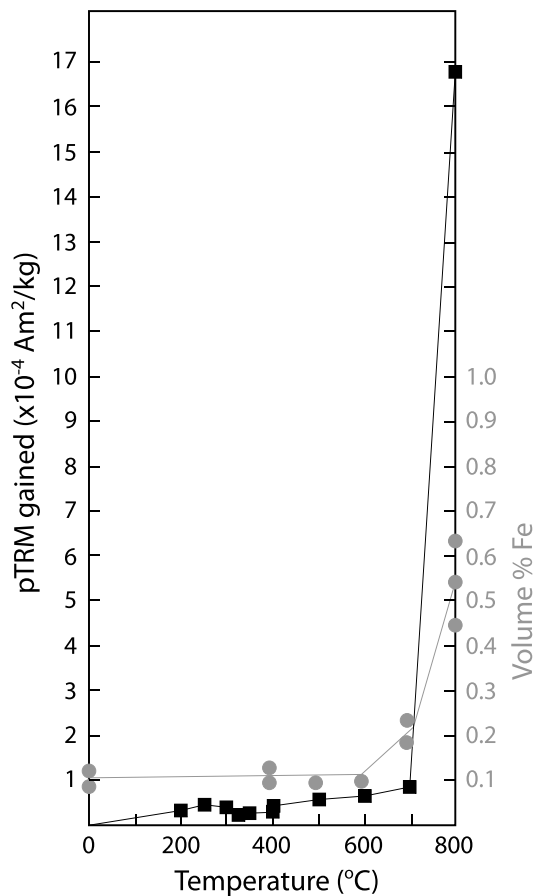


Figure 9. Magnetic enhancement through heating experiments on a synthetic lunar sample. Black squares represent the amount of partial thermoremanent magnetization (pTRM) gained by the sample after heating to different temperatures. Gray circles represent the inferred metallic Fe content in the sample following each heating step. Modified from Pearce et al. (1976).

this alteration to reach its maximum extent. Pearce et al. (1976) also reported that the reduction of troilite in their experiments produced a modest (<10%) increase in the abundance of metallic iron.

More recently, Tikoo et al. (2014) conducted several heating experiments on ilmenite basalt 12022 using the controlled fO_2 (IW-1) H_2 - CO_2 atmosphere oven system described by Suavet et al. (2014). This system has been used successfully to retrieve paleointensities from mare basalt analogs (Suavet et al., 2014) as well as impact melt rock portions of a lunar regolith breccia (Tikoo et al., 2017), with limited sample alteration as constrained by pTRM checks (after Tauxe & Staudigel, 2004). The experiments by Suavet et al. (2014) produced Fe from ilmenite, with the Fe grains ranging from submicron to a few microns in size—large compared to the single domain to pseudosingle domain size transition of ~ 25 nm for cubic Fe grains—suggesting that the Fe grains produced by the reduction mechanisms discussed here are probably multidomain grains. Some of the heating experiments on 12022 (not all of which were presented by Tikoo et al., 2014, but are included here) involved imparting subsamples of the rock with laboratory IRM acquired in a near-saturating 886.5-mT field before or after heating the subsamples for 20 min to temperatures of 575–600 °C. The mean intensities of the laboratory IRMs acquired after heating were a factor of ~ 3 higher than those acquired by unheated subsamples (Figure 10). These experiments suggest that heating-related reduction of ilmenite and troilite led to the formation of additional metal within subsamples of 12022. In summary, experimental evidence indicates that heating lunar rocks to temperatures of at least 575 °C in a reducing environment facilitates the creation of new ferromagnetic grains, providing a mechanism for enhancing rock magnetization within and near intrusive bodies.

3.2. Heating by Dikes and Lava Tubes

Many of the Moon’s crustal magnetic anomalies, including the Reiner Gamma anomaly, are located within, or in proximity to, mare plains with maximum thicknesses of a few kilometers. These mare plains were likely fed via intrusions and lava tubes that contained material that originated from mantle sources and were emplaced shallowly. The dikes associated

with mare volcanism are generally inferred to have lengths ranging from tens to hundreds of kilometers and widths of tens of meters to ~ 250 m (Head & Wilson, 1993; Wilson & Head, 1981). Much wider dikes (tens of kilometers wide) may also exist, such as those inferred to exist on the lunar nearside in the substructure of the Procellarum region (Andrews-Hanna et al., 2014). Collapsed lunar lava tubes have been observed to have widths of up to ~ 3 km, although the vast majority have widths < 1.5 km (e.g., Hadley Rille is ~ 1.2 km wide; Howard et al., 1972). Dikes form relatively rapidly, having typical emplacement timescales of minutes to days (Montgomery-Brown et al., 2010; Spence & Turcotte, 1985). In contrast, lava tubes may serve as magma conduits for months (Calvari & Pinkerton, 1998, 1999). The emplacement of these dikes and lava tubes could account for the strong magnetization of swirl-bearing magnetic anomalies provided that either the bodies themselves acquire a strong magnetization or that sufficient volumes of the adjacent rocks are raised to sufficiently high temperatures.

Here we use a heat conduction model to determine the extent of the region that is heated to at least 600 °C following the emplacement of a dike or flowing lava tube. We assume a lunar surface temperature of $T_s = -20$ °C and apply a geothermal gradient of $\frac{dT}{dz} = 13.5$ °C/km (approximated by averaging the initial and current model mantle temperature profiles from Laneville et al., 2013) to determine preintrusion temperatures of host rocks, given by

$$T_{\text{host}}(x, z) = T_s + \frac{dT}{dz}z \quad (7)$$

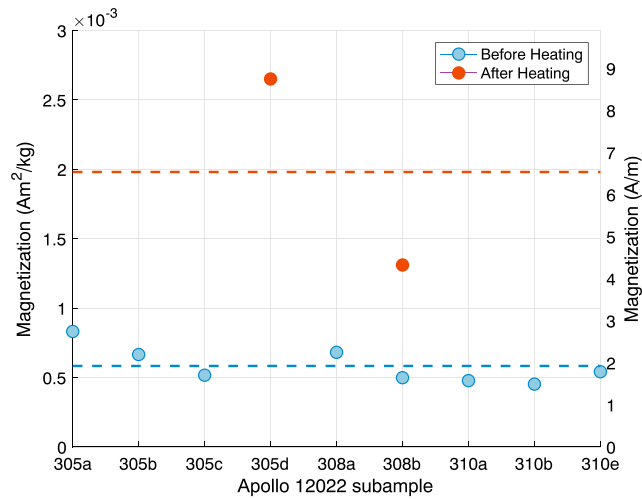


Figure 10. Magnetization intensities for Apollo 12022 subsamples that were imparted with 886.5-mT isothermal remanent magnetization before and/or after heating to 575–600 °C. Dashed lines illustrate mean values before and after heating. The right scale shows the conversion to units of amperes per meter assuming a rock density of 3,300 kg/m³.

where x is the horizontal position with respect to the center of the intrusion and z is the depth. Assuming mainly horizontal heat flow away from the intrusion, we compute the temperature field at time t according to (e.g., Delaney, 1987)

$$T(x, z, t) = T_{\text{host}}(x, z) + (T_0 - T_{\text{host}}(x, z)) \frac{1}{2} \left(\operatorname{erf} \left(\frac{\frac{b}{2} + x}{\sqrt{4\kappa t}} \right) + \operatorname{erf} \left(\frac{\frac{b}{2} - x}{\sqrt{4\kappa t}} \right) \right) \quad (8)$$

where κ is the thermal diffusivity, which we take to be 10^{-6} m²/s for the intrusion and the host rock alike, b is the width of the hot magmatic body, and T_0 is its initial temperature. As end member scenarios we assume initial temperatures of either 1200 or 1500 °C. These temperatures lie within the 1100–1500 °C range of liquidus temperatures determined for lunar mare basalts (Wieczorek et al., 2001). High temperatures (~1500 °C) may also be achieved by emplacement of ultramafic komatiites, which may have formed on the Moon in rare circumstances (Green, 1972; Ringwood et al., 1987).

Intrusions are treated here as instantaneous heat pulses, with heat then diffusing into the surrounding host rock as the body cools. For various depths and widths, we determine peak temperatures experienced in and around the magmatic body following its initial emplacement by evaluating (8) at a series of times in steps of at most 100 years (peak temperatures are reached within a few thousand years). Peak rock temperature is a strong function of the initial temperature and width of the intrusive body (i.e., the amount of thermal energy deposited) as well as distance away from the body (Figure 11a). The width of the heated region is also a weak function of depth (Figure 11b). With an initial temperature of 1200 °C, host rock temperatures do not exceed 600 °C except within a few meters of the intrusion. With initial temperatures of 1500 °C, however, the region heated to at least 600 °C extends some 20% beyond the body's own width.

Small-scale swirls (e.g., $L = 1$ km or less) are readily accounted for by shallow dikes or lava tubes, provided those dikes or lava tubes are not too wide (see Figure 4a). Conversely, for the largest-scale swirls, the corresponding magmatic bodies must not be too narrow either. This is because very narrow sources can give rise to large transition length scales only if they are deeply buried (Figure 4a), which in turn requires strong rock magnetization (Figure 4b). For example, with $L = 5$ km, a 100-m-wide dike with an aspect ratio $h/w = 10$, has $w/L = 0.02$ and $d/L \approx 0.9$ and requires the rock magnetization to exceed 300 A/m assuming a surface field of 300 nT. On the other hand, the same result is achieved with < 1 A/m given a 1500 °C, 2,000-m-wide dike, which heats a region ~ 2.5 km wide, yielding $w/L = 0.5$ and $d/L \approx 0.18$. Lava tubes could also account for some of the larger-scale swirl features if they are sufficiently large and/or deeply buried. For example, a 3-km diameter lava tube that is initially flowing with $T_0 = 1500$ °C heats a region roughly 3.5 km \times 3.5 km. If the top of this region is 3 km beneath the surface, then the result (neglecting the cross-sectional differences between lava tubes and the prism represented in Figure 3) is $L \approx 4.8$ km ($w/L \approx 0.74$, $d/L \approx 0.63$). To produce a 300-nT field at the surface, the corresponding rock magnetization would have to be ~ 2.8 A/m.

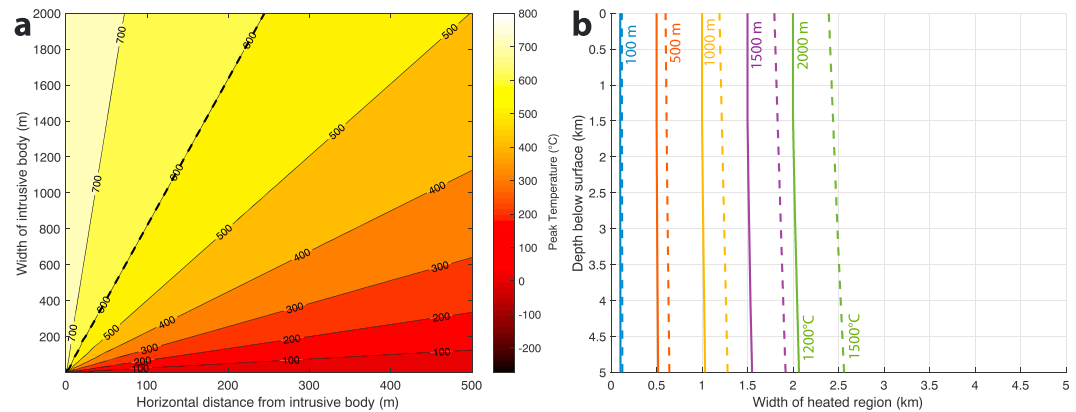


Figure 11. (a) Peak temperatures reached in the vicinity of a cooling magmatic body as a function of the body's width, shown here for the example case of an initial temperature of 1500 °C and measured at a depth of 3 km. The dashed line marks the region heated to at least 600 °C. (b) Width of the heated region (the intrusion plus the part of the surrounding host rock that is heated to at least 600 °C) as a function of depth and shown for a series of different intrusion widths (from 100 to 2,000 m) and shown for two different initial temperatures: 1200 °C (solid lines) and 1500 °C (dashed lines).

The preceding analysis assumed an instantaneous heat pulse into an otherwise cold host rock, which may be a good assumption for dikes that are isolated in space and time. Although lava tubes may remain active for months, an instantaneous heat pulse may nevertheless be an appropriate assumption in the case of deeply buried lava tubes, for which the thermal diffusion timescale could be relatively long (e.g., for a depth of 1 km, the diffusion timescale is $> 10^4$ years). On the other hand, the assumption of an initially cold host rock is conservative in the sense that it neglects the possibility of residual heat from previous episodes of intrusive activity. That is, the volume of rock heated to at least 600 °C could be considerably larger in regions where previously used magmatic pathways are periodically reactivated.

As discussed in section 3.1, temperatures of 600 °C are sufficient to thermochemically alter host rocks and form new ferromagnetic grains. Because temperatures of several hundred degrees Celsius may persist for $> 10^3$ years (far longer than laboratory heating timescales), there is ample opportunity to pervasively reduce minerals such as ilmenite and troilite in mare basalts, as well as thermally remagnetize host rocks (Garrick-Bethell & Weiss, 2010). If such thermochemical alteration and cooling occur in the presence of a stable dynamo field, preexisting and neoformed ferromagnetic grains may acquire a mixture of TRM and TCRM that could be orders of magnitude more intense than the primary magnetizations of unaltered rocks. Such a process would result in a substantial magnetization contrast between altered rocks and their unaltered surroundings, producing a magnetic anomaly.

If dikes and lava tubes are indeed the origin of these swirl bearing magnetic anomalies, the natural limits on their depths and widths may effectively limit the scale of swirls, potentially explaining why their bright-to-dark transition length scales rarely exceed ~ 5 km. Given that most known lunar dikes have widths < 250 m and given that lava tube depths are not likely to exceed ~ 2 km, the conditions necessary for making the largest swirl-bearing magnetic anomalies may be present only in rare circumstances. This may also help account for why it is that lunar swirls and strong crustal magnetic anomalies are not found everywhere across the mare plains, in spite of the fact that lunar magmatism and the dynamo persisted for over two billion years after the formation of the Moon. Similarly, modest variations in oxygen fugacity between magma sources (stemming from lunar mantle heterogeneity) may cause rocks forming in some locations to be more reduced and metal rich than rocks forming in other locations. Finally, the intensity of magnetization in a host rock depends strongly on the intensity of the ambient magnetic field in which its ferromagnetic grains were magnetized. Rocks magnetized during the lunar high field period (between at least 3.85 and 3.56 Ga) are more likely to carry strong magnetizations than older rocks that formed before the high field period or younger rocks that formed after the lunar dynamo declined.

4. Conclusions

Following from several magnetometer-based studies of magnetic field structure (Hemingway & Garrick-Bethell, 2012; Shibuya et al., 2010; Tsunakawa et al., 2015), together with a series of hybrid and

kinetic plasma simulations (e.g., Bamford et al., 2012, 2016; Deca et al., 2016; Poppe et al., 2012, 2016; Zimmerman et al., 2015), we use lunar swirl morphology as a proxy for the structure of near-surface magnetic fields. This allows us to place strong constraints on the geometry of the underlying magnetic source bodies. Incorporating conservative estimates of near-surface field strength (Tsunakawa et al., 2015), we additionally place constraints on the intensity of magnetization in these source bodies (Figure 5). We conclude that, at least where lunar swirls are present, the underlying magnetic source bodies must be narrow, elongate structures, whose upper surfaces must be shallow (less than 0.5–2.5 km below the surface), with magnetization intensities of at least 0.5 A/m and perhaps closer to ~ 2 A/m or even more.

Although their fine scale and complexity has made it difficult to characterize swirl-bearing magnetic anomalies comprehensively, magnetometer-based inversions of isolated anomalies, such as Airy and Reiner Gamma, support our suggestion of elongate sources (with widths less than the spacecraft altitude), even when the optical features are ignored (e.g., Hemingway & Garrick-Bethell, 2012; Oliveira & Wiczorek, 2017). The requirement of narrow, shallow sources may account for why it is that not all crustal magnetic anomalies are accompanied by swirls. If they are not sufficiently shallow and narrow, even strong crustal magnetic anomalies (e.g., the Mare Crisium anomalies) will not produce the very strong near surface fields and spatially rapidly varying field orientations required to produce swirls (section 2.3 and Figure 6).

Our result also sheds light on the possible origins of the magnetic anomalies accompanying lunar swirls (section 2.4 and Figure 8). In particular, we argue that magnetization of mare basalt flows, impact melt sheets, or rocks that experienced cometary collisions, is unlikely to produce the narrow, elongate magnetic source bodies required to account for the near-surface magnetic field structure that gives rise to swirls. In terms of magnetization intensity, impact ejecta deposits, especially if they are enriched in metals, may be good candidates for the sources underlying swirls, although it is not obvious how well they can account for swirl morphology. Dikes and lava tubes, on the other hand, readily account for the narrow and often sinuous morphology of lunar swirl complexes. The natural limits on their depths and widths may also account for why the bright-to-dark transition length scales of swirls rarely exceed ~ 5 km.

The main challenge with the dike and lava tube hypotheses is that they require a process that could enhance the metal content to substantially beyond what is currently represented in the sample record. In section 3, we showed that subsolidus reduction of minerals such as ilmenite and chromite during deuteric cooling may lead to elevated metal contents and, in turn, strong remanent magnetization within intruding magmatic bodies. We also showed that the emplacement of dikes or lava tubes could heat the surrounding rocks enough to impart them with additional TRM and/or TCRM that could be an order of magnitude more intense than the primary remanence found in lunar basalts. The largest swirls, however, require large and/or high-temperature (~ 1500 °C) magmatic bodies, which may be rare. Further studies regarding the range of conditions that could allow for the formation of strong magnetic carriers could be an important part of accounting for the presence and distribution of lunar crustal magnetic anomalies.

Appendix A: Source Geometry and Surface Fields

The vector magnetic field arising from a magnetic dipole moment, $\mathbf{m} = [m_x \ m_y \ m_z]^T$, is given by (e.g., Blakely, 1995)

$$\mathbf{B}(\mathbf{r}) = \frac{\mu_0}{4\pi} (3(\mathbf{m} \cdot \mathbf{r})\mathbf{r} - m^2\mathbf{r}) \frac{1}{r^5} \quad (\text{A1})$$

where $\mathbf{r} = [r_x \ r_y \ r_z]^T$ is the vector position of the evaluation point with respect to the location of the magnetic dipole.

We will use a coordinate system whose x-y plane coincides with the surface and whose z axis points upward. Consider a buried magnetized rectangular prism that is infinitely long in the y direction and symmetric about the y-z plane. If the prism has width w (in the x direction), height h (in the z direction), and is buried a depth d below the surface (Figure 3), then the magnetic field can be obtained by integrating equation (A1) over the prism's volume. We will focus on the two end member cases of horizontal (parallel to the x axis) and vertical (parallel to the z axis) magnetization, always in the plane of Figure 3. Since we assume that the source has infinite extent parallel to the y axis, magnetization components parallel to the y axis do not contribute to the external magnetic field.

A1. Horizontal Magnetization

Supposing that the magnetization (magnetic moment per unit volume) is purely in the +x direction, that is, $\mathbf{M} = [M \ 0 \ 0]^T$, where M is the magnitude of the magnetization (A/m). In this case, the contribution from each infinitesimal volume element in the source is

$$\mathbf{B}(\mathbf{r}) = \frac{\mu_0}{4\pi} \left(3Mr_x \begin{bmatrix} r_x \\ r_y \\ r_z \end{bmatrix} (r_x^2 + r_y^2 + r_z^2)^{-5/2} - \begin{bmatrix} M \\ 0 \\ 0 \end{bmatrix} (r_x^2 + r_y^2 + r_z^2)^{-3/2} \right) dr_x dr_y dr_z \quad (\text{A2})$$

Considering the x component of the vector field at a position (x, z) , we have

$$B_x(x, z) = M \frac{\mu_0}{4\pi} \int \int \int \left(3r_x^2 (r_x^2 + r_y^2 + r_z^2)^{-5/2} - (r_x^2 + r_y^2 + r_z^2)^{-3/2} \right) dr_x dr_y dr_z \quad (\text{A3})$$

where if the volume element is located at x', y' , and z' , then $r_x = x - x'$, $r_y = y - y'$, and $r_z = z - z'$, so that $dr_x = -dx'$, $dr_y = -dy'$, and $dr_z = -dz'$. The integration in y' is from $-\infty$ to ∞ , the integration in x' is from one face of the prism ($x' = -w/2$) to the other ($x' = w/2$), and the integration in z' is from the top of the prism ($z' = -d$) to the bottom ($z' = -(d + h)$). After integrating, we obtain

$$B_x(x, z) = M \frac{\mu_0}{2\pi} \left(\arctan \left(\frac{z+d}{x+w/2} \right) - \arctan \left(\frac{z+d+h}{x+w/2} \right) \dots \right. \\ \left. - \arctan \left(\frac{z+d}{x-w/2} \right) + \arctan \left(\frac{z+d+h}{x-w/2} \right) \right) \quad (\text{A4})$$

At the origin, this simplifies to

$$B_x(0, 0) = M \frac{\mu_0}{\pi} \left(\arctan \left(\frac{d}{w/2} \right) - \arctan \left(\frac{d+h}{w/2} \right) \right) \quad (\text{A5})$$

By symmetry, the vector field has no y component ($B_y(x, z) = 0$).

Considering the z component of the vector field at a position (x, z) , we have

$$B_z(x, z) = M \frac{\mu_0}{4\pi} \int \int \int \left(3r_x r_z (r_x^2 + r_y^2 + r_z^2)^{-5/2} \right) dr_x dr_y dr_z \quad (\text{A6})$$

where the integration limits are as above. After integrating, we obtain

$$B_z(x, z) = M \frac{\mu_0}{4\pi} \ln \left[\left(\frac{(x+w/2)^2 + (z+d+h)^2}{(x+w/2)^2 + (z+d)^2} \right) \left(\frac{(x-w/2)^2 + (z+d)^2}{(x-w/2)^2 + (z+d+h)^2} \right) \right] \quad (\text{A7})$$

At the origin, $B_z(0, 0) = 0$, meaning the field is purely horizontal. Using (A7), it can be shown that $B_z = 0$ whenever $x = 0$ as well as whenever $z = -(d + h/2)$. Using (A4), it can be shown that the field is vertical, that is, $B_x = 0$, whenever

$$(x + w/2)(x - w/2) = (z + d)(z + d + h) \quad (\text{A8})$$

A2. Vertical Magnetization

Supposing that the magnetization is instead in the +z direction, that is, $\mathbf{M} = [0 \ 0 \ M]^T$, where M is the magnitude of the magnetization (A/m). In this case, we have

$$\mathbf{B}(\mathbf{r}) = \frac{\mu_0}{4\pi} \left(3Mr_z \begin{bmatrix} r_x \\ r_y \\ r_z \end{bmatrix} (r_x^2 + r_y^2 + r_z^2)^{-5/2} - \begin{bmatrix} 0 \\ 0 \\ M \end{bmatrix} (r_x^2 + r_y^2 + r_z^2)^{-3/2} \right) dr_x dr_y dr_z \quad (\text{A9})$$

The x component of the field is given by

$$B_x(x, z) = M \frac{\mu_0}{4\pi} \int \int \int \left(3r_z r_x (r_x^2 + r_y^2 + r_z^2)^{-5/2} \right) dr_x dr_y dr_z \quad (\text{A10})$$

After integrating over the volume of the source body, we obtain

$$B_x(x, z) = M \frac{\mu_0}{4\pi} \ln \left[\left(\frac{(x + w/2)^2 + (z + d + h)^2}{(x + w/2)^2 + (z + d)^2} \right) \left(\frac{(x - w/2)^2 + (z + d)^2}{(x - w/2)^2 + (z + d + h)^2} \right) \right] \quad (\text{A11})$$

which is identical to (A7).

The z component of the field is given by

$$B_z(x, z) = M \frac{\mu_0}{4\pi} \int \int \int \left(3r_z^2 (r_x^2 + r_y^2 + r_z^2)^{-5/2} - (r_x^2 + r_y^2 + r_z^2)^{-3/2} \right) dr_x dr_y dr_z \quad (\text{A12})$$

After integrating over the volume of the source body, we obtain

$$B_z(x, z) = M \frac{\mu_0}{2\pi} \left(\arctan \left(\frac{x + w/2}{z + d} \right) - \arctan \left(\frac{x + w/2}{z + d + h} \right) \dots \right. \\ \left. - \arctan \left(\frac{x - w/2}{z + d} \right) + \arctan \left(\frac{x - w/2}{z + d + h} \right) \right) \quad (\text{A13})$$

which differs from (A4) only because the integration limits are different in the x and z directions. However, using the identity $\arctan \left(\frac{1}{\alpha} \right) = \frac{\pi}{2} - \arctan(\alpha)$, this can also be written as

$$B_z(x, z) = -M \frac{\mu_0}{2\pi} \left(\arctan \left(\frac{z + d}{x + w/2} \right) - \arctan \left(\frac{z + d + h}{x + w/2} \right) \dots \right. \\ \left. - \arctan \left(\frac{z + d}{x - w/2} \right) + \arctan \left(\frac{z + d + h}{x - w/2} \right) \right) \quad (\text{A14})$$

which differs from (A4) only in its sign. At the origin, this again simplifies to

$$B_z(0, 0) = -M \frac{\mu_0}{\pi} \left(\arctan \left(\frac{d}{w/2} \right) - \arctan \left(\frac{d + h}{w/2} \right) \right) \quad (\text{A15})$$

Using (A11), it can be shown that the field is vertical, that is, $B_x = 0$, whenever $x = 0$ as well as whenever $z = -(d + h/2)$. Using (A13), it can be shown that the field is horizontal, that is, $B_z = 0$, whenever

$$(x + w/2)(x - w/2) = (z + d)(z + d + h), \quad (\text{A16})$$

which is identical to (A8).

A3. Transition Length Scale

When the magnetization is horizontal, the field direction transitions from horizontal at $(x, z) = (0, 0)$ to vertical at $(x, z) = (L, 0)$, where L is obtained by setting (A4) to zero and solving. Similarly, when the magnetization is vertical, the field direction transitions from vertical at $(x, z) = (0, 0)$ to horizontal at $(x, z) = (L, 0)$, where L is obtained by setting (A13) to zero and solving. In either case, we obtain L by solving (A8) for x with $z = 0$. The result is

$$L = \sqrt{(d + h)d + (w/2)^2} \quad (\text{A17})$$

regardless of whether the magnetization direction is horizontal or vertical.

It follows from (A17) that $d < L$ for all positive h and w and that $w < 2L$ for all $d > 0$. It can be shown that the width to depth ratio (w/d) can be written in terms of the dimensionless quantities of prism aspect ratio (h/w) and relative burial depth (d/L) as

$$\frac{w}{d} = 2 \sqrt{\left(\frac{h}{w} \right)^2 - \left(1 - \left(\frac{L}{d} \right)^2 \right) - \left(\frac{h}{w} \right)} \quad (\text{A18})$$

Substitution of (A18) into (A5) helpfully allows all the important relationships to be captured in terms of dimensionless quantities. The resulting expression for the magnitude of the magnetic field at the origin, relative to the source magnetization, is

$$\frac{B}{M} = \frac{\mu_0}{\pi} \left[\arctan \left(\frac{(d/L)}{\sqrt{\left(\frac{d}{L}\right)^2 \left(\frac{h}{w}\right)^2 + \left(1 - \left(\frac{d}{L}\right)^2\right) - \left(\frac{h}{w}\right) \left(\frac{d}{L}\right)}}\right) + \left(\frac{h}{w/2}\right) \dots \right. \\ \left. - \arctan \left(\frac{(d/L)}{\sqrt{\left(\frac{d}{L}\right)^2 \left(\frac{h}{w}\right)^2 + \left(1 - \left(\frac{d}{L}\right)^2\right) - \left(\frac{h}{w}\right) \left(\frac{d}{L}\right)}}\right) \right] \quad (\text{A19})$$

which, again, holds regardless of whether the magnetization direction is horizontal or vertical.

Acknowledgments

This paper benefitted from insightful and constructive reviews by Catherine Johnson and an anonymous reviewer. We also thank Michael Manga, Ian Garrick-Bethell, Tushar Mittal, Andrew Poppe, Claude Herzberg, and Juliane Gross for helpful comments and suggestions. We thank Brett Denevi and Mark Wieczorek for supplying their swirl and source depth maps, respectively. We thank Benjamin Weiss for access to rock magnetic data from Apollo sample 12022 that was previously acquired by the MIT Paleomagnetism Laboratory. All other data and models are freely available in the published literature. D. J. H. was supported by the Miller Institute for Basic Research in Science at the University of California Berkeley. S. M. T. was supported by the Rutgers University School of Arts and Sciences.

References

- Andrews-Hanna, J. C., Besserer, J., Head, III, J. W., Howett, C. J. A., Kiefer, W. S., Lucey, P. J., et al. (2014). Structure and evolution of the lunar procellarum region as revealed by GRAIL gravity data. *Nature*, *514*(7520), 68–71. <https://doi.org/10.1038/nature13697>
- Bamford, R. A., Alves, E. P., Cruz, F., Kellett, B. J., Fonseca, R. A., Silva, L. O., et al. (2016). 3D pic simulations of collisionless shocks at lunar magnetic anomalies and their role in forming lunar swirls. *The Astrophysical Journal*, *830*(2), 146. <https://doi.org/10.3847/0004-637X/830/2/146>
- Bamford, R. A., Kellett, B., Bradford, W. J., Norberg, C., Thornton, A., Gibson, K. J., et al. (2012). Mini-magnetospheres above the lunar surface and the formation of lunar swirls. *Physical Review Letters*, *109*(8), 81101.
- Blakely, R. J. (1995). *Potential theory in gravity and magnetic applications*. Cambridge: Cambridge University Press.
- Blewett, D. T., Coman, E. I., Hawke, B. R., Gillis-Davis, J. J., Purucker, M. E., & Hughes, C. G. (2011). Lunar swirls: Examining crustal magnetic anomalies and space weathering trends. *Journal of Geophysical Research*, *116*, E02002. <https://doi.org/10.1029/2010JE003656>
- Buchan, K. L. (2007). Baked Contact Test. In D. Gubbins & E. Herrero-Bervera (Eds.), *Encyclopedia of geomagnetism and paleomagnetism, Encyclopedia of Earth Sciences Series* (p. 1054). Dordrecht, Netherlands: Springer.
- Calvari, S., & Pinkerton, H. (1998). Formation of lava tubes and extensive flow field during the 1991–1993 eruption of Mount Etna. *Journal of Geophysical Research*, *103*(B11), 27,291–27,301. <https://doi.org/10.1029/97JB03388>
- Calvari, S., & Pinkerton, H. (1999). Lava tube morphology on Etna and evidence for lava flow emplacement mechanisms. *Journal of Volcanology and Geothermal Research*, *90*(3–4), 263–280. [https://doi.org/10.1016/S0377-0273\(99\)00024-4](https://doi.org/10.1016/S0377-0273(99)00024-4)
- Coe, R. S., Jarboe, N. A., Le Goff, M., & Petersen, N. (2014). Demise Of the rapid-field-change hypothesis at Steens Mountain: The crucial role of continuous thermal demagnetization. *Earth and Planetary Science Letters*, *400*, 302–312. <https://doi.org/10.1016/j.epsl.2014.05.036>
- Deca, J., Divin, A., Lembège, B., Horányi, M., Markidis, S., & Lapenta, G. (2015). General mechanism and dynamics of the solar wind interaction with lunar magnetic anomalies from 3-D particle-in-cell simulations. *Journal of Geophysical Research: Space Physics*, *120*, 6443–6463. <https://doi.org/10.1002/2015JA021070>
- Deca, J., Divin, A., Wang, X., Lembège, B., Markidis, S., Horányi, M., & Lapenta, G. (2016). 3-D full-kinetic simulation of the solar wind interaction with a vertical dipolar lunar magnetic anomaly. *Geophysical Research Letters*, *43*, 4136–4144. <https://doi.org/10.1002/2016GL068535>
- Delaney, P. T. (1987). Heat transfer during emplacement and cooling of mafic dykes. In H. C. Halls & W. Fahrig (Eds.), *Mafic Dyke Swarms* (pp. 31–46). St. John's Newfoundland: Geological Association of Canada.
- Denevi, B. W., Robinson, M. S., Boyd, A. K., Blewett, D. T., & Klima, R. L. (2016). The distribution and extent of lunar swirls. *Icarus*, *273*, 53–67. <https://doi.org/10.1016/j.icarus.2016.01.017>
- Dowty, E., Prinz, M., & Keil, K. (1973). Composition, mineralogy, and petrology of 28 mare basalts from Apollo 15 rake samples. *Proceedings of the Fourth Lunar Science Conference*, *1*, 423–444.
- Dwyer, C. A., Stevenson, D. J., & Nimmo, F. (2011). A long-lived lunar dynamo driven by continuous mechanical stirring. *Nature*, *479*(7372), 212–214. <https://doi.org/10.1038/nature10564>
- Dyal, P., Parkin, C. W., & Daily, W. D. (1974). Magnetism and the interior of the Moon. *Reviews of Geophysics*, *12*(4), 568–591. <https://doi.org/10.1029/RG012i004p00568>
- El-Baz, F. (1972). The Alhazen to Abul Wafa swirl belt: An extensive field of light-colored sinuous markings, *Apollo 16: Preliminary Science Report. NASA SP-315, C-3 Pages*. Washington, D.C.: NASA, pp. 29–93.
- Evans, A. J., Zuber, M. T., Weiss, B. P., & Tikoo, S. M. (2014). A wet, heterogeneous lunar interior: Lower mantle and core dynamo evolution. *Journal of Geophysical Research: Planets*, *119*, 1061–1077. <https://doi.org/10.1002/2013JE004494>
- Everitt, C. W. F., & Clegg, J. A. (1962). A field test of palaeomagnetic stability. *Geophysical Journal of the Royal Astronomical Society*, *6*(3), 312–319. <https://doi.org/10.1111/j.1365-246X.1962.tb00354.x>
- Fatemi, S., Lue, C., Holmström, M., Poppe, A. R., Wieser, M., Barabash, S., & Delory, G. T. (2015). Solar wind plasma interaction with Gerasimovich lunar magnetic anomaly. *Journal of Geophysical Research: Space Physics*, *120*, 4719–4735. <https://doi.org/10.1002/2015JA021027>
- Garrick-Bethell, I., Head, J. W., & Pieters, C. M. (2011). Spectral properties, magnetic fields, and dust transport at lunar swirls. *Icarus*, *212*(2), 480–492. <https://doi.org/10.1016/j.icarus.2010.11.036>
- Garrick-Bethell, I., & Weiss, B. P. (2010). Kamacite blocking temperatures and applications to lunar magnetism. *Earth and Planetary Science Letters*, *294*(1–2), 1–7. <https://doi.org/10.1016/j.epsl.2010.02.013>
- Gattacceca, J., & Rochette, P. (2004). Toward a robust normalized magnetic paleointensity method applied to meteorites. *Earth and Planetary Science Letters*, *227*(3–4), 377–393. <https://doi.org/10.1016/j.epsl.2004.09.013>

- Giacalone, J., & Hood, L. L. (2015). Hybrid simulation of the interaction of solar wind protons. *Journal of Geophysical Research: Space Physics*, 120, 4081–4094. <https://doi.org/10.1002/2014JA020938>
- Gose, W. A., & Butler, R. F. (1975). Magnetism of the moon and meteorites. *Reviews of Geophysics*, 13(3), 189–193. <https://doi.org/10.1029/RG013i003p00189>
- Green, D. H. (1972). Archaean greenstone belts may include terrestrial equivalents of lunar maria? *Earth and Planetary Science Letters*, 15, 263–270.
- Haggerty, S. E. (1971). Subsolidus reduction of lunar spinels. *Nature Physical Science*, 234, 113–117.
- Halekas, J. S., Lillis, R. J., Lin, R. P., Manga, M., Purucker, M. E., & Carley, R. A. (2010). How strong are lunar crustal magnetic fields at the surface? Considerations from a reexamination of the electron reflectometry technique. *Journal of Geophysical Research*, 115, E03006. <https://doi.org/10.1029/2009JE003516>
- Halekas, J. S., Mitchell, D. L., Lin, R. P., Frey, S., Hood, L. L., Acuña, M. H., & Binder, A. B. (2001). Mapping of crustal magnetic anomalies on the lunar near side by the Lunar Prospector electron reflectometer. *Journal of Geophysical Research*, 106(E11), 841–852.
- Hapke, B. (2001). Space weathering from Mercury to the asteroid belt. *Journal of Geophysical Research*, 106(E5), 10,039–10,073.
- Head, J. W., & Wilson, L. (1993). Lunar graben formation due to near-surface deformation accompanying dike emplacement. *Planetary and Space Science*, 41(10), 719–727. [https://doi.org/10.1016/0032-0633\(93\)90114-H](https://doi.org/10.1016/0032-0633(93)90114-H)
- Hemingway, D., & Garrick-Bethell, I. (2012). Magnetic field direction and lunar swirl morphology: Insights from Airy and Reiner Gamma. *Journal of Geophysical Research*, 117, E10012. <https://doi.org/10.1029/2012JE004165>
- Hodge, K. F., Carazzo, G., Montague, X., & Jellinek, A. M. (2012). Magmatic structures in the Tuolumne Intrusive Suite, California: A new model for the formation and deformation of ladder dikes. *Contributions to Mineralogy and Petrology*, 164(4), 587–600. <https://doi.org/10.1007/s00410-012-0760-6>
- Hood, L. L., & Artemieva, N. A. (2008). Antipodal effects of lunar basin-forming impacts: Initial 3D simulations and comparisons with observations. *Icarus*, 193(2), 485–502. <https://doi.org/10.1016/j.icarus.2007.08.023>
- Hood, L. L., & Schubert, G. (1980). Lunar magnetic anomalies and surface optical properties. *Science*, 208, 49–51. <https://doi.org/10.1126/science.208.4439.49>
- Hood, L., & Williams, C. (1989). The lunar swirls—Distribution and possible origins. In *19th Lunar and Planetary Science Conference* (Vol. 19, pp. 99–113). Houston, TX.
- Howard, K. A., Head, J. W., & Swann, G. A. (1972). *Interagency report: 41: Geology of Hadley Rille: Preliminary report*. Washington, DC: United States Department of the Interior Geological Survey.
- Humm, D. C., Tschimmel, M., Brylow, S. M., Mahanti, P., Tran, T. N., Braden, S. E., et al. (2016). Flight calibration of the LROC narrow angle camera. *Space Science Reviews*, 200(1–4), 431–473. <https://doi.org/10.1007/s11214-015-0201-8>
- Jarvinen, R., Alho, M., Kallio, E., Wurz, P., Barabash, S., & Futaana, Y. (2014). On vertical electric fields at lunar magnetic anomalies. *Geophysical Research Letters*, 41, 2243–2249. <https://doi.org/10.1002/2014GL059788>
- Kent, D. V., & Gee, J. (1996). Magnetic alteration of zero-age oceanic basalt. *Geology*, 24(8), 703–706. [https://doi.org/10.1130/0091-7613\(1996\)024<0703:MAOZAO>2.3.CO;2](https://doi.org/10.1130/0091-7613(1996)024<0703:MAOZAO>2.3.CO;2)
- Kiefer, W. S., Macke, R. J., Britt, D. T., Irving, A. J., & Consolmagno, G. J. (2012). The density and porosity of lunar rocks. *Geophysical Research Letters*, 39, L07201. <https://doi.org/10.1029/2012GL051319>
- Kurata, M., Tsunakawa, H., Saito, Y., Shibuya, H., Matsushima, M., & Shimizu, H. (2005). Mini-magnetosphere over the Reiner Gamma magnetic anomaly region on the Moon. *Geophysical Research Letters*, 32, L24205. <https://doi.org/10.1029/2005GL024097>
- Laneuville, M., Wicczorek, M. A., Breuer, D., Aubert, J., Morard, G., & Rückriemen, T. (2014). A long-lived lunar dynamo powered by core crystallization. *Earth and Planetary Science Letters*, 401, 251–260. <https://doi.org/10.1016/j.epsl.2014.05.057>
- Laneuville, M., Wicczorek, M. A., Breuer, D., & Tosi, N. (2013). Asymmetric thermal evolution of the Moon. *Journal of Geophysical Research: Planets*, 118, 1435–1452. <https://doi.org/10.1002/jgre.20103>
- Le Bars, M., Wicczorek, M. A., Karatekin, Ö, Cébron, D., & Laneuville, M. (2011). An impact-driven dynamo for the early Moon. *Nature*, 479(7372), 215–218. <https://doi.org/10.1038/nature10565>
- Longhi, J., Walker, D., Grove, T. L., Stolper, E. M., & Hays, J. F. (1974). The petrology of the Apollo 17 mare basalts. *Proceedings of the Fifth Lunar Conference*, 1, 447–469.
- Mahanti, P., Humm, D. C., Robinson, M. S., Boyd, A. K., Stelling, R., Sato, H., et al. (2016). Inflight Calibration of the Lunar Reconnaissance Orbiter Camera Wide Angle Camera. *Space Science Reviews*, 200(1–4), 393–430. <https://doi.org/10.1007/s11214-015-0197-0>
- Mitchell, D., Halekas, J., Lin, R., Frey, S., Hood, L., Acuña, M., & Binder, A. (2008). Global mapping of lunar crustal magnetic fields by Lunar Prospector. *Icarus*, 194(2), 401–409. <https://doi.org/10.1016/j.icarus.2007.10.027>
- Montgomery-Brown, E. K., Sinnott, D. K., Poland, M., Segall, P., Orr, T., Zebker, H., & McKliis, A. (2010). Geodetic evidence for an echelon dike emplacement and concurrent slow slip during the June 2007 intrusion and eruption at Kilauea volcano, Hawaii. *Journal of Geophysical Research*, 115, B07405. <https://doi.org/10.1029/2009JB006658>
- Neal, C. R., Hacker, M. D., Snyder, G. A., Taylor, L. A., Liu, Y.-G., & Schmitt, R. A. (1994). Basalt generation at the Apollo 12 site, Part 1: New data, classification, and re-evaluation. *Meteoritics*, 29, 334–348.
- Nicholis, M. G., & Rutherford, M. J. (2009). Graphite oxidation in the Apollo 17 orange glass magma: Implications for the generation of a lunar volcanic gas phase. *Geochimica et Cosmochimica Acta*, 73(19), 5905–5917. <https://doi.org/10.1016/j.gca.2009.06.022>
- Noble, S. K., Pieters, C. M., Taylor, L. A., Morris, R. V., Allen, C. C., McKay, D. S., & Keller, L. P. (2001). The optical properties of the finest fraction of lunar soil: Implications for space weathering. *Meteoritics & Planetary Science*, 36, 31–42.
- Oliveira, J. S., & Wicczorek, M. A. (2017). Testing the axial dipole hypothesis for the Moon by modeling the direction of crustal magnetization. *Journal of Geophysical Research: Planets*, 122, 383–399. <https://doi.org/10.1002/2016JE005199>
- Oliveira, J. S., Wicczorek, M. A., & Kletetschka, G. (2017). Iron abundances in lunar impact basin melt sheets from orbital magnetic field data. *Journal of Geophysical Research: Planets*, 122, 2429–2444. <https://doi.org/10.1002/2017JE005397>
- Pearce, G. W., Hoyer, G. S., Strangway, D. W., Walker, B. M., & Taylor, L. A. (1976). Some complexities in the determination of lunar paleointensities. *Proceedings of the Lunar Science Conference 7th*, 3, 3271–3297.
- Pieters, C. M., Moriarty, D. P., & Garrick-Bethell, I. (2014). Atypical regolith processes hold the key to enigmatic lunar swirls. 45th Lunar and Planetary Science Conference.
- Poppe, A. R., Fatemi, S., Garrick-Bethell, I., Hemingway, D., & Holmström, M. (2016). Solar Wind interaction with the Reiner Gamma crustal magnetic anomaly: Connecting source magnetization to surface weathering. *Icarus*, 266, 261–266. <https://doi.org/10.1016/j.icarus.2015.11.005>
- Poppe, A. R., Halekas, J. S., Delory, G. T., & Farrell, W. M. (2012). Particle-in-cell simulations of the solar wind interaction with lunar crustal magnetic anomalies: Magnetic cusp regions. *Journal of Geophysical Research*, 117, A09105. <https://doi.org/10.1029/2012JA017844>

- Purucker, M. E., Head, J. W., & Wilson, L. (2012). Magnetic signature of the lunar South Pole-Aitken basin: Character, origin, and age. *Journal of Geophysical Research*, *117*, E05001. <https://doi.org/10.1029/2011JE003922>
- Purucker, M. E., & Nicholas, J. B. (2010). Global spherical harmonic models of the internal magnetic field of the Moon based on sequential and coestimation approaches. *Journal of Geophysical Research*, *115*, E12007. <https://doi.org/10.1029/2010JE003650>
- Richmond, N. C., & Hood, L. L. (2008). A preliminary global map of the vector lunar crustal magnetic field based on Lunar Prospector magnetometer data. *Journal of Geophysical Research*, *113*, E02010. <https://doi.org/10.1029/2007JE002933>
- Ringwood, A. E., Seifert, S., & Wänke, H. (1987). A komatiite component in Apollo 16 highland breccias: Implications for the nickel-cobalt systematics and bulk composition of the Moon. *Earth and Planetary Science Letters*, *81*, 105–117. [https://doi.org/10.1016/0012-821X\(87\)90149-X](https://doi.org/10.1016/0012-821X(87)90149-X)
- Robinson, M. S., Brylow, S. M., Tschimmel, M., Humm, D., Lawrence, S. J., Thomas, P. C., et al. (2010). Lunar Reconnaissance Orbiter Camera (LROC) instrument overview. *Space Science Reviews*, *150*(1–4), 81–124. <https://doi.org/10.1007/s11214-010-9634-2>
- Rochette, P., Gattacceca, J., Ivanov, A. V., Nazarov, M. A., & Bezaeva, N. S. (2010). Magnetic properties of lunar materials: Meteorites, Luna and Apollo returned samples. *Earth and Planetary Science Letters*, *292*(3–4), 383–391. <https://doi.org/10.1016/j.epsl.2010.02.007>
- Sato, M., Hickling, N. L., & McLane, J. E. (1973). Oxygen fugacity values of Apollo 12, 14, and 15 lunar samples and reduced state of lunar magmas. *Proceedings of the Fourth Lunar Science Conference*, *4*, 1061.
- Scheinberg, A. L., Soderlund, K. M., & Elkins-Tanton, L. T. (2018). A basal magma ocean dynamo to explain the early lunar magnetic field. *Earth and Planetary Science Letters*, *492*, 144–151. <https://doi.org/10.1016/j.epsl.2018.04.015>
- Scheinberg, A., Soderlund, K. M., & Schubert, G. (2015). Magnetic field generation in the lunar core: The role of inner core growth. *Icarus*, *254*, 62–71. <https://doi.org/10.1016/j.icarus.2015.03.013>
- Schultz, P. H., & Srnka, L. J. (1980). Cometary collisions on the Moon and Mercury. *Nature*, *284*, 22–26.
- Shau, Y.-H., Torii, B. M., Homg, C.-S., & Peacor, D. R. (2000). Subsolvus evolution and alteration of titanomagnetite in ocean ridge basalts from Deep Sea Drilling Project/Ocean Drilling Program Hole 504B, Leg 83: Implications for the timing of magnetization. *Journal of Geophysical Research*, *105*(B10), 23,635–23,649. <https://doi.org/10.1029/2000JB900191>
- Shau, Y.-h., Torii, M., Horng, C.-s., & Liang, W.-T. (2004). Magnetic properties of mid-ocean-ridge basalts from Ocean Drilling Program leg 187. In *Proceedings of the Ocean Drilling Program*, *187*, 1–25.
- Shibuya, H., Tsunakawa, H., Takahashi, F., Shimizu, H., Matsushima, M., & Team, K. M.-L. (2010). Near surface magnetic field mapping over the swirls in the SPA region using Kaguya LMAG data. In *European Planetary Science Congress*, *5*, GP42A-03.
- Spence, D. A., & Turcotte, D. L. (1985). Magma-driven propagation of cracks. *Journal of Geophysical Research*, *90*(B1), 575–580.
- Speyerer, E. J., Wagner, R. V., Robinson, M. S., Humm, D. C., Becker, K., Anderson, J., & Thomas, P. (2012). In-flight geometric calibration of the Lunar Reconnaissance Orbiter Camera. In *International Archives of the Photogrammetry, Remote Sensing and Spatial Information Sciences*, pp. 511–516.
- Srnka, L. J. (1977). Spontaneous magnetic field generation in hypervelocity impacts. In *Procedures of 8th Lunar Science Conference*, pp. 785–792.
- Stegman, D. R., Jellinek, A. M., Zatman, S. A., Baumgardner, J. R., & Richards, M. A. (2003). An early lunar core dynamo driven by thermochemical mantle convection. *Nature*, *421*(6919), 143–146. <https://doi.org/10.1038/nature01267>
- Suavet, C., Weiss, B. P., & Grove, T. L. (2014). Paleointensity analyses of extraterrestrial rocks. *Geochemistry, Geophysics, Geosystems*, *15*, 2733–2743. <https://doi.org/10.1002/2013GC005215>
- Syal, M. B., & Schultz, P. H. (2015). Cometary impact effects at the Moon: Implications for lunar swirl formation. *Icarus*, *257*, 194–206. <https://doi.org/10.1016/j.icarus.2015.05.005>
- Tauxe, L., & Staudigel, H. (2004). Strength of the geomagnetic field in the Cretaceous Normal Superchron: New data from submarine basaltic glass of the Troodos Ophiolite. *Geochemistry, Geophysics, Geosystems*, *5*, Q02H06. <https://doi.org/10.1029/2003GC000635>
- Thellier, E. (1959). Sur l'intensité du champ magnétique terrestre dans le passé historique et géologique. *Annales Geophysicae*, *15*, 285–376.
- Tikoo, S. M., Gattacceca, J., Swanson-hysell, N. L., Weiss, B. P., Suavet, C., & Cournède, C. (2015). Preservation and detectability of shock-induced magnetization. *Journal of Geophysical Research: Planets*, *120*, 1461–1475. <https://doi.org/10.1002/2015JE004840>
- Tikoo, S. M., Weiss, B. P., Cassata, W. S., Shuster, D. L., Gattacceca, J. Ô., Lima, E. A., et al. (2014). Decline Of the lunar core dynamo. *Earth and Planetary Science Letters*, *404*, 89–97. <https://doi.org/10.1016/j.epsl.2014.07.010>
- Tikoo, S. M., Weiss, B. P., Shuster, D. L., Suavet, C., Wang, H., & Grove, T. L. (2017). A two-billion-year history for the lunar dynamo. *Science Advances*, *3*(8), e1700207. <https://doi.org/10.1126/sciadv.1700207>
- Tsunakawa, H., Takahashi, F., Shimizu, H., Shibuya, H., & Matsushima, M. (2015). Surface vector mapping of magnetic anomalies over the Moon using Kaguya and Lunar Prospector observations. *Journal of Geophysical Research: Planets*, *120*, 1160–1185. <https://doi.org/10.1002/2014JE004785>
- Weiss, B. P., & Tikoo, S. M. (2014). The lunar dynamo. *Science*, *346*(6214), 1246753. <https://doi.org/10.1126/science.1246753>
- Wieczorek, M. A. (2018). Strength, depth, and geometry of magnetic sources in the crust of the Moon from localized power spectrum analysis. *Journal of Geophysical Research: Planets*, *123*, 291–316. <https://doi.org/10.1002/2017JE005418>
- Wieczorek, M. A., Weiss, B. P., & Stewart, S. T. (2012). An impactor origin for lunar magnetic anomalies. *Science*, *335*(6073), 1212–1215. <https://doi.org/10.1126/science.1214773>
- Wieczorek, M. A., Zuber, M. T., & Phillips, R. J. (2001). The role of magma buoyancy on the eruption of lunar basalts. *Earth and Planetary Science Letters*, *185*(1–2), 71–83. [https://doi.org/10.1016/S0012-821X\(00\)00355-1](https://doi.org/10.1016/S0012-821X(00)00355-1)
- Wilson, L., & Head, J. W. (1981). Ascent and eruption of basaltic magma on the Earth and Moon. *Journal of Geophysical Research*, *86*(B4), 2971–3001. <https://doi.org/10.1029/JB086iB04p02971>
- Xu, W., Van der Voo, R., Peacor, D. R., & Beaubouef, R. T. (1997). Alteration and dissolution of fine-grained magnetite and its effects on magnetization of the ocean floor. *Earth and Planetary Science Letters*, *151*, 279–288. [https://doi.org/https://doi.org/10.1016/S0012-821X\(97\)81854-7](https://doi.org/https://doi.org/10.1016/S0012-821X(97)81854-7)
- Zimmerman, M. L., Farrell, W. M., & Poppe, A. R. (2015). Kinetic simulations of kilometer-scale mini-magnetosphere formation on the Moon. *Journal of Geophysical Research: Planets*, *120*, 1893–1903. <https://doi.org/10.1002/2015JE004865>